Sparse modeling study of extracting charmonium spectral functions from lattice QCD at finite temperature

Junichi Takahashi*
Meteorological College, Japan Meteorological Agency, 7-4-81, Asahi-cho, Kashiwa, Chiba 277-0852, Japan

Hiroshi Ohno†
Center for Computational Sciences, University of Tsukuba, 1-1-1, Tennodai, Tsukuba, Ibaraki 305-8577, Japan

Akio Tomiya‡
Department of Information and Mathematical Sciences, Division of Mathematical Sciences, Tokyo Women's Christian University, 2-6-1 Zempukuji, Suginami-ku, Tokyo 167-8585, Japan, RIKEN Center for Computational Science, Kobe 650-0047, Japan, and Department of Physics, Kyoto University, Kyoto 606-8502, Japan

(Received 3 October 2025; accepted 28 January 2026; published 23 February 2026)

We present charmonium spectral functions extracted from Euclidean-time correlation functions using sparse modeling (SpM). SpM solves inverse problems by considering only the sparsity of the target solution. To assess the applicability of the method, we first test it with mock data designed to mimic charmonium correlation functions. We demonstrate that while resonance peaks in the spectral functions can be reconstructed using this method, transport peaks are difficult to resolve without introducing further assumptions beyond sparsity. We then apply the method to charmonium correlation functions obtained from lattice quantum chromodynamics (QCD) at temperatures below and above the critical temperature. The results are found to be qualitatively consistent with those obtained using the maximum entropy method, although the transport peak is not clearly resolved. This indicates that, even when relying solely on the assumption of sparsity, the method can capture some relevant features of the underlying physics.

DOI: 10.1103/cdjf-65yf

I. INTRODUCTION

Meson spectral functions provide essential information on the properties of hot and dense quantum chromodynamics (QCD) matter created in relativistic heavy-ion collisions. They encode the real-time dynamics of strongly interacting systems and are directly related to phenomenologically relevant observables. For example, the vector spectral function determines the thermal dilepton production rate [1–3], which offers an experimentally accessible probe of the electromagnetic response of the quark-gluon plasma (QGP).

Quarkonium, a bound state of a heavy quark and antiquark, serves as a valuable probe of QGP created in relativistic heavy-ion collisions [4]. Due to the large quark mass, quarkonium systems can be described within a nonrelativistic framework, which allows us to relate their in-medium properties to an effective heavy-quark potential. At finite temperature, this potential becomes complex-valued, reflecting the interaction of the heavy quark–antiquark pair with the surrounding thermal medium [5–9]. The real part of the potential is modified by the presence of color charges in the deconfined medium, leading to color Debye screening of the quark-antiquark interaction. As the temperature increases, this screening weakens the binding of quarkonium states. In addition, the imaginary part of the finite-temperature potential encodes medium-induced dissociation processes, such as Landau damping and singlet-octet transitions caused by interactions with thermal gluons. These effects give rise to a finite thermal width of quarkonium states, implying that quarkonium melting should be understood not only as the disappearance of bound states due to screening, but also as the loss of well-defined resonances caused by strong in-medium damping.

Experimental studies at RHIC and LHC have provided compelling evidence for such in-medium modifications of

*Contact author: mhjkk-takahashi@met.kishou.go.jp
†Contact author: hohno@ccs.tsukuba.ac.jp
‡Contact author: akio@yukawa.kyoto-u.ac.jp

quarkonia. Measurements of the J/Ψ and Υ yields reveal significant suppression compared to the proton-proton baselines [10–14]. These measurements provide essential information on the onset of deconfinement and the properties of the QGP, and motivate further theoretical studies to understand the in-medium modification of quarkonium, requiring knowledge of the corresponding spectral function. Beyond quarkonium spectroscopy, the low-frequency structure of the vector spectral function is directly related to transport coefficients such as the heavy quark diffusion constant [15], which are essential to describe transport phenomena in heavy-ion experiments.

In lattice QCD, however, spectral functions cannot be computed directly. Instead, they are inferred from meson correlation functions in Euclidean time. Reconstructing spectral functions from these correlation functions is, however, an ill-posed inverse problem: the limited number of temporal data points and the presence of statistical noise make it difficult to uniquely determine the spectral shape.

Various approaches have been proposed to address this difficulty, including the maximum entropy method (MEM) [16], the Backus-Gilbert method [17], the Chybyshev polynomial method [18], and stochastic methods [19]. Each of these has its strengths and limitations, and the results may depend sensitively on algorithmic choices. For this reason, it is necessary to compare different reconstruction methods in order to assess systematic uncertainties.

Recently, sparse modeling (SpM) has been introduced to the lattice QCD community as a promising alternative for spectral reconstruction. Originally developed in condensed matter physics [20,21], it enables stable reconstructions with reduced bias and controlled resolution, while relying on fewer explicit model assumptions compared to conventional approaches. In particular, Itou and Nagai [22] successfully applied SpM to the correlation functions of the energy–momentum tensor, demonstrating its potential to extract transport coefficients such as shear viscosity. Motivated by the question of whether essential quarkonium physics can be extracted within a framework with minimal model assumptions, we adopt SpM in this study. Extending this approach to the study of quarkonium correlators at finite temperature provides a new opportunity to obtain more reliable information on in-medium spectral functions, including quarkonium survival patterns and transport properties relevant for heavy-ion phenomenology.

In this work, we investigate the charmonium spectral function at finite temperature using SpM. By performing analyses with both mock data and data from lattice QCD calculations and by comparing our results with conventional methods, we assess systematic uncertainties and establish the applicability of SpM for quantitative studies of heavy-quark observables in the QGP.

The remainder of the paper is organized as follows. In Sec. II, we give a brief review of the SpM method, explain our ideas and describe the procedure for using the method to extract spectral functions in our study. In Sec. III, we explain the mock-data tests of the method and discuss the results of that test. Section IV presents the results of the spectral functions using actual lattice QCD data. Finally, we summarize our study in Sec. V.

II. SPARSE MODELING

In this section, we introduce the SpM method. In Sec. II A, we briefly review its formulation in the intermediate representation (IR) basis, following Refs. [20,23]. While previous studies have generally neglected the covariance between correlation functions at different Euclidean times, SpM is capable of incorporating it [23], and we explicitly take this covariance into account in our analysis, as explained in Sec. II B. Finally, because the method is employed here to extract spectral functions from correlation functions, the corresponding formalism and procedure are presented in Sec. II C.

A. Brief review of the sparse modeling method

Extracting spectral functions by using SpM has been proposed in condensed matter physics [20,21]. Following Ref. [23] which provides a more detailed review, we give a brief review on formulation of the SpM method in the IR basis.

Euclidean formulation of lattice QCD cannot directly determine the meson spectral function $\rho(\omega)$ at the frequency ω; instead, one can measure the meson correlation function $G(\tau)$ at the Euclidean time τ. $G(\tau)$ and $\rho(\omega)$ can be written in Lehmann representation in the following form

$$G(\tau) = \int_0^\infty d\omega K(\tau,\omega)\rho(\omega), \tag{1}$$

by using the Kubo-Martin-Schwinger relation and the periodic boundary condition of $G(\tau)$. Here, $K(\omega,\tau)$ is the integration kernel represented in the following form

$$K(\tau,\omega) = \frac{\cosh\left[\omega(\tau-\frac{1}{2T})\right]}{\sinh(\frac{\omega}{2T})}, \tag{2}$$

in the Euclidean time range $0 \le \tau \le 1/T$ with temperature T. Note that the kernel $K(\tau,\omega)$ is symmetric around $\tau = 1/(2T)$ and the spectral function $\rho(\omega)$ is an odd function of the frequency ω. This means that $\rho(\omega)$ holds

$$\frac{\rho(\omega)}{\omega} \ge 0. \tag{3}$$

Equations (1) and (2) are used as clues to determine $\rho(\omega)$ using $G(\tau)$ as the input data.

In numerical calculations the Euclidean time τ and the frequency ω must be discretized. The length in the Euclidean-time direction is limited by the lattice size of the lattice simulations, and we introduce a cutoff $\omega_{\max}$ for the infinite

integral over ω. Then the variable τ and ω are discretized into M and N slices, respectively. Defining $G_i \equiv G(\tau_i)$ and $\rho_i \equiv \rho(\omega_i)\Delta\omega$ where $\Delta\omega$ is the interval of ω instead of $d\omega$, we can denote Eq. (1) using a matrix-vector representation

$$\vec{G} = K\vec{\rho}. \tag{4}$$

Here, K is an $M \times N$ matrix defined by $K_{ij} \equiv K(\tau_i, \omega_j)$.

To find $\vec{\rho}$, we consider the square error

$$\chi^2(\vec{\rho}|\vec{G}) = \frac{1}{2}\|\vec{G} - K\vec{\rho}\|_2^2, \tag{5}$$

and minimize it. Here, the argument on the left-hand side of the bar ($\vec{\rho}$) indicates a quantity to be varied, that on the right-hand side of the bar ($\vec{G}$) indicates a fixed quantity and $\|\cdot\|_2$ stands for the L_2 norm defined by

$$\|\vec{\rho}\|_2 \equiv \left(\sum_j \rho_j^2\right)^{1/2}. \tag{6}$$

Since we now assuming that $N > M$, the number of Eq. (4) is insufficient for $\vec{\rho}$ to be determined uniquely. We could solve the equation if $N = M$, while $\vec{G}$ has a noise, and it is difficult to obtain the stable solution of $\vec{\rho}$.

To address these difficulties we take an efficient basis that yields a sparse solution. Here, "sparse" is such that most components of the solution are zero. If we can find the position of zeros in the components and remove these zeros from the set of equations, the number of components will be reduced, and then equations are solvable if $N = M$.

For the realization of this situation, we first decompose the kernel K using the singular value decomposition (SVD) as

$$K = USV^{\mathrm{t}}, \tag{7}$$

where the superscript t indicates transpose, S is an $M \times N$ matrix composed of singular values $s_l (l = 1, 2, \ldots, M)$ at the diagonal, and U and V are $M \times M$ and $N \times N$ orthogonal matrices, respectively. Here, the sequence $\{s_l\}$ is sorted by magnitude in descending order. Then we transform the vectors $\vec{G}$ and $\vec{\rho}$ using the orthogonal matrices U and V as

$$\vec{G}' \equiv U^{\mathrm{t}}\vec{G}, \qquad \vec{\rho}' \equiv V^{\mathrm{t}}\vec{\rho}, \tag{8}$$

respectively. This new basis is called intermediate representation (IR) basis. Rewriting the square error in Eq. (5) with the new vectors, $\vec{G}'$ and $\vec{\rho}'$, in the IR basis, we obtain

$$\chi^2(\vec{\rho}'|\vec{G}') = \frac{1}{2}\|\vec{G}' - S\vec{\rho}'\|_2^2 \tag{9}$$

$$= \frac{1}{2}\sum_l (G_l' - s_l\rho_l')^2. \tag{10}$$

Thus minimizing $\chi^2(\vec{\rho}'|\vec{G}')$ is to find a solution that satisfies the equation

$$G_l' = s_l\rho_l'. \tag{11}$$

Note that the singular values s_l for the type of kernel described by Eq. (2) decrease exponentially.

We focus on the property of s_l. G_l' can decay much faster than ρ_l' due to the behavior of s_l, which relies on the nature of the kernel K. Thus, the fast decay of G_l' does not depend on a simulation detail. It indicates that G_l' does not include information about ρ_l' at large l. In other words, elements of G_l', s_l and ρ_l' can be removed at large l. It is called "dimensionality reduction" in Ref. [23]. This reduction is a good solution for the inverse problem we address, which involves correlation functions with noise as input. Equation (11) shows that $\rho(\omega)$ and $G(\tau)$ are directly connected to each other in the IR basis, and $\rho(\omega)$ could be naively evaluated by using the relation

$$\rho_l' = G_l'/s_l. \tag{12}$$

This evaluation, however, does not work well due to noise of $G(\tau)$. Even if the noise in $G(\tau)$ is small, its influence is amplified at large l, as Eq. (12) shows. On the other hand, the influences of noise can be mitigated by the reduction.

In actual calculations, thresholds s_{cut} are set for the obtained singular values s_l, taking into account the properties described above. We can discard such a component corresponding to $l > l_{\mathrm{cut}}$ below this threshold, $s_l < s_{\mathrm{cut}}$. This truncation is necessary to obtain a stable solution against the noise in $G(\tau)$.

After dimensionality reduction, imposing sparseness on $\vec{\rho}'$ to obtain a stable solution against noise, we introduce the L_1 regularization term to $\chi^2(\vec{\rho}'|\vec{G}')$ as

$$F(\vec{\rho}'|\vec{G}', \lambda) \equiv \chi^2(\vec{\rho}'|\vec{G}') + \lambda\|\vec{\rho}'\|_1, \tag{13}$$

where λ is a positive hyperparameter which controls the contribution of L_1 regularization relative to $\chi^2(\vec{\rho}'|\vec{G}')$, and $||\cdot||_1$ stands for the L_1 norm defined by

$$\|\vec{\rho}'\|_1 \equiv \sum_l |\rho_l'|. \tag{14}$$

The L_1 regularization makes the solution sparse and remove irrelevant bases. Thus the parameter λ regulates the degree of sparseness. The optimal value of λ can be automatically determined as will be mentioned in Sec. II C. This minimization problem, expressed by Eq. (13), is known as the least absolute shrinkage and selection operator (LASSO). Given that the LASSO is a convex optimization problem, the global minimum can be achieved regardless of initial conditions [24].

The solution will hold two additional constraints. One is the non-negativity condition of the spectral function,

$$\rho_j \geq 0. \tag{15}$$

This condition is imposed in this study. The other is the sum rule,

$$\sum_j \rho_j = 1, \tag{16}$$

while this condition is not imposed in this study. With these additional constraints, the minimization problem in Eq. (13) can be solved using the alternating direction method of multipliers (ADMM) algorithm [25]. For the detail of the algorithm, see Appendix A.

B. Consideration of covariance matrices for sparse modeling

In practical simulations, we obtain the Monte Carlo data $\vec{G}$ with noise which is the source of the statistical error, and $\vec{G}$ has correlation between different Euclidean times. Thus the covariance of $\vec{G}$ should be taken into account. In this case Ref. [23] explains that the square error in Eq. (5) can be extent to a form,

$$\chi^2(\vec{\rho}|\vec{G}, C) = \frac{1}{2}(\vec{G} - K\vec{\rho})^{\mathrm{t}} C^{-1}(\vec{G} - K\vec{\rho}), \tag{17}$$

where C represents the covariance matrix defined by

$$C_{ij} = \frac{1}{N_{\mathrm{conf}}(N_{\mathrm{conf}} - 1)} \times \sum_{n=1}^{N_{\mathrm{conf}}} (G_i - G_i^{(n)})(G_j - G_j^{(n)}), \tag{18}$$

$$G_i = \frac{1}{N_{\mathrm{conf}}} \sum_{n=1}^{N_{\mathrm{conf}}} G_i^{(n)}, \tag{19}$$

where N_{conf} is the total number of gauge configurations and $G_i^{(n)}$ is the value of the correlation function measured on the nth gauge configuration.

Since the covariance matrix C is a symmetric matrix, its inverse is also symmetric and can be factorized using the Cholesky decomposition as

$$C^{-1} = W^{\mathrm{t}} W, \tag{20}$$

where W is the upper triangular matrix. Using Eq. (20) and defining

$$\vec{G}_W \equiv W\vec{G}, \qquad K_W \equiv WK, \tag{21}$$

we can rewrite Eq. (17) as

$$\chi^2(\vec{\rho}|\vec{G}_W) = \frac{1}{2}\|\vec{G}_W - K_W\vec{\rho}\|_2^2. \tag{22}$$

Now that we have the squared error such as Eq. (5), by decomposing K_W using SVD as

$$K_W = U_W S_W V_W^{\mathrm{t}}, \tag{23}$$

where S_W is an $M \times N$ matrix composed singular values, and U_W and V_W are $M \times M$ and $N \times N$ orthogonal matrices, respectively, and defining new vectors in the IR basis as

$$\vec{G}'_W \equiv U_W^{\mathrm{t}}\vec{G}_W, \qquad \vec{\rho}'_W \equiv V_W^{\mathrm{t}}\vec{\rho}, \tag{24}$$

we can express the squared error

$$\chi^2(\vec{\rho}'_W|\vec{G}'_W) = \frac{1}{2}\|\vec{G}'_W - S_W\vec{\rho}'_W\|_2^2, \tag{25}$$

in the IR basis. The optimization problem to find a sparse solution of $\vec{\rho}'_W$ can be solved using

$$F(\vec{\rho}'_W|\vec{G}'_W, \lambda) \equiv \chi^2(\vec{\rho}'_W|\vec{G}'_W) + \lambda\|\vec{\rho}'_W\|_1, \tag{26}$$

with two additional constraints in Eqs. (15) and (16).

In order to use dimensionality reduction, it is necessary that the components of S_W decrease exponentially. We make sure that in the Appendix B.

C. Formalism of sparse modeling for extraction of spectral functions

Here we present the SpM formalism to extract spectral functions from correlation functions obtained by lattice calculations.

The starting point of the formalism is Eq. (1). According to the detailed formulation described in Appendix C, Eq. (1) can be written as

$$\hat{G}(\hat{\tau}_i) = \sum_{j=0}^{N_\omega - 1} K^{(0)}(\hat{\tau}_i, \hat{\omega}_j)\tilde{\rho}^{(0)}(\hat{\omega}_j), \tag{27}$$

$$K^{(0)}(\hat{\tau}_i, \hat{\omega}_j) = \sqrt{\Delta\omega'}\hat{\omega}_{\max} \frac{\cosh[\hat{\omega}_j(\hat{\tau}_i - N_\tau/2)]}{\cosh[\hat{\omega}_j(\hat{\tau}_{\mathrm{r}} - N_\tau/2)]}, \tag{28}$$

$$\tilde{\rho}^{(0)}(\hat{\omega}_j) = \sqrt{\Delta\omega'} \frac{\cosh[\hat{\omega}_j(\hat{\tau}_{\mathrm{r}} - N_\tau/2)]}{\sinh(\hat{\omega}_j N_\tau/2)} \hat{\rho}(\hat{\omega}_j), \tag{29}$$

where hatted variables are dimensionless quantities, N_ω is the number of points in ω-space, $\Delta\omega' \equiv 1/(N_\omega - 1)$, $\hat{\omega}_{\max}$ is a cutoff for $\hat{\omega}$, N_τ is the extent of Euclidean times and $\hat{\tau}_{\mathrm{r}}$ is the reference Euclidean time. In this study, we extract $\tilde{\rho}^{(0)}(\hat{\omega}_j)$ directly from correlation functions using ADMM algorithm for $K^{(0)}(\hat{\tau}_i, \hat{\omega}_j)$.

Note that $\tilde{\rho}^{(0)}(\hat{\omega}_j)$ in Eq. (29) is proportional to $\hat{\rho}(\hat{\omega}_j)/\hat{\omega}_j$ in the limit $\hat{\omega} \to 0$. One method of investigating the transport properties at temperatures above T_{c} is to examine the transport peak of the spectral function. Theoretically, the transport peak has a finite value in $\hat{\rho}(\hat{\omega}_j)/\hat{\omega}_j$ at $\hat{\omega} \to 0$.

Thus, it is favorable to find the equivalent of $\hat{\rho}(\hat{\omega}_j)/\hat{\omega}_j$ directly using ADMM algorithm from the outset, and $\tilde{\rho}^{(0)}(\hat{\omega}_j)$ in Eq. (29) is of that form.

At temperatures below T_c, $\hat{\rho}(\hat{\omega}_j)$ is expected to be asymptotically proportional to $\hat{\omega}^2$ in high frequency region. Therefore, the resonance peak is usually checked by $\hat{\rho}(\hat{\omega}_j)/\hat{\omega}_j^2$. Thus, it is favorable to find the equivalent of $\hat{\rho}(\hat{\omega}_j)/\hat{\omega}_j^2$ directly using ADMM algorithm. In addition, a transport peak for the spectral function is expected to not appear at $\omega \to 0$ at temperatures below T_c. Taken these features into consideration, Eqs. (27)–(29) can be rewritten as

$$\hat{G}(\hat{\tau}_i) = \sum_{j=0}^{N_\omega - 1} K^{(1)}(\hat{\tau}_i, \hat{\omega}_j)\tilde{\rho}^{(1)}(\hat{\omega}_j), \tag{30}$$

$$K^{(1)}(\hat{\tau}_i, \hat{\omega}_j) = \sqrt{\Delta\omega'}\hat{\omega}_j\hat{\omega}_{\max}\frac{\cosh\left[\hat{\omega}_j(\hat{\tau}_i - N_\tau/2)\right]}{\cosh\left[\hat{\omega}_j(\hat{\tau}_r - N_\tau/2)\right]}, \tag{31}$$

$$\tilde{\rho}^{(1)}(\hat{\omega}_j) = \sqrt{\Delta\omega'}\frac{\cosh\left[\hat{\omega}_j(\hat{\tau}_r - N_\tau/2)\right]}{\sinh\left(\hat{\omega}_j N_\tau/2\right)}\frac{\hat{\rho}(\hat{\omega}_j)}{\hat{\omega}_j}. \tag{32}$$

$K^{(1)}(\hat{\tau}_i, \hat{\omega}_j)$ incorporates an additional $\hat{\omega}_j$ with respect to $K^{(0)}(\hat{\tau}_i, \hat{\omega}_j)$, and $\tilde{\rho}^{(0)}(\hat{\omega}_j)$ is divided by $\hat{\omega}_j$ to yield $\tilde{\rho}^{(1)}(\hat{\omega}_j)$.

Note that $\tilde{\rho}^{(1)}(0) = 0$ is obtained in SpM analysis. Since $K^{(1)}(\hat{\tau}_i, 0) = 0$, $\tilde{\rho}^{(1)}(0)$ does not contribute to the correlation function. Conversely, the values of $\tilde{\rho}^{(1)}(0)$ cannot be constrained from the given data. On the other hand, attempting to set $\tilde{\rho}^{(1)}(0)$ to a nonzero value inevitably increases the error function due to the L_1 regularization term. Therefore, the most favorable solution is to set $\tilde{\rho}^{(1)}(0)$ to zero. Furthermore, due to dimensionality reduction, SpM uses only the minimum necessary modes, and high-frequency modes sensitive to noise are prioritize for removal during this process. Thus, sharp structures requiring many high-frequency modes are less likely to appear, and a smooth spectral function can be obtained. Consequently, $\tilde{\rho}^{(1)}(\hat{\omega}_j)$ smoothly approaches zero near $\hat{\omega} = 0$. Based on these considerations, in this study, $\tilde{\rho}^{(1)}(\hat{\omega}_j)$ is also extracted directly from correlation functions at temperature below T_c using ADMM algorithm for $K^{(1)}(\hat{\tau}_i, \hat{\omega}_j)$. However, it is clear that $K^{(1)}(\hat{\tau}_i, \hat{\omega}_j)$ should not be employed in analyses at temperature above T_c, where a transport peak is expected to exist.

The covariance matrix C is considered in our SpM analyses. To account for the covariance in the actual calculation, rewriting K_W defined in Eq. (21), we define $K_W^{(n)}(\hat{\tau}_k, \hat{\omega}_j)$ as

$$K_W^{(n)}(\hat{\tau}_k, \hat{\omega}_j) \equiv \sum_{i=0}^{N_\tau - 1} W(\hat{\tau}_k, \hat{\tau}_i)K^{(n)}(\hat{\tau}_i, \hat{\omega}_j), \tag{33}$$

where $n = 0$, 1 and the matrix $W(\hat{\tau}_k, \hat{\tau}_i)$ is obtained from the Cholesky decomposition of C^{-1} as

$$C^{-1}(\hat{\tau}_k, \hat{\tau}_l) = \sum_{m=0}^{N_\tau - 1} W(\hat{\tau}_m, \hat{\tau}_k)W(\hat{\tau}_m, \hat{\tau}_l), \tag{34}$$

which is rewritten from Eq. (20).

D. Procedure of sparse modeling for extraction of spectral functions

Now, we summarize the SpM procedure in this study. The following procedure assumes that the correlation functions $\hat{G}(\hat{\tau}_i)$ have been obtained by lattice calculation, and superscripts (n) introduced in Sec. II C are omitted here for simplicity.

(1) Calculate the covariance matrix C from the correlation functions $\hat{G}(\hat{\tau}_i)$, carry out the Cholesky decomposition of the inverse of C and obtain the matrix W.
(2) Construct the discretized kernel K_W using the kernel K and W.
(3) Perform SVD of the kernel K_W.
(4) Transform the basis of $\hat{G}(\hat{\tau}_i)$ and $\tilde{\rho}(\hat{\omega}_j)$ by U_W^t and V_W^t to obtain $G'_W(\hat{\tau}_i)$ and $\rho'_W(\hat{\omega}_j)$ in IR basis.
(5) Choose up to Lth largest singular values satisfied with the condition $s_l/s_1 \geq 10^{-15}$, where s_l is the lth largest singular value, and drop the components of $G'_W(\hat{\tau}_i)$ and $\rho'_W(\hat{\omega}_j)$ corresponding to the other small singular values, which reduces the size of U_W, V_W and S_W to $N_\tau \times L$, $N_\omega \times L$ and $L \times L$, respectively.
(6) Construct the cost function $F(\rho'_W(\hat{\omega}_j)|G'_W(\hat{\tau}_i), \lambda)$ from the square error $\chi^2(\rho'_W(\hat{\omega}_j)|G'_W(\hat{\tau}_i))$ and the L_1 regularization term.
(7) Estimate the optimal value of λ, λ_{opt}, in the same way as in the previous study [22], which is explained in detail in Appendix D.
(8) Find the most likely spectral function $\rho'_W(\hat{\omega}_j)$ in IR basis by minimizing the cost function $F(\rho'_W(\hat{\omega}_j)|G'_W(\hat{\tau}_i), \lambda_{\text{opt}})$ using the ADMM algorithm, transform the basis of $\rho'_W(\hat{\omega}_j)$ by V_W to obtain $\tilde{\rho}(\hat{\omega}_j)$ and calculate $\hat{\rho}(\hat{\omega}_j)$.

III. MOCK DATA ANALYSIS

In this section we show the results of the mock-data tests using SpM. As mentioned above, SpM has been applied to correlation functions computed on actual lattice QCD data only in a few cases, and meson spectral functions at finite T have not yet been computed by using this method. Therefore, before we analyze the actual lattice QCD data of meson correlation functions by using SpM, we first test the method with mock data that mimic possible charmonium spectral functions.

Since we are interested in the applicability of this method to meson correlation functions, we will prepare spectral functions that reproduce correlation functions close to those computed for lattice QCD. This spectral function is shown in Sec. III A. Another aspect is applicability with respect to the number of data points and the quality of the data.

The results of these investigations are discussed in Sec. III B. A further aspect examined in this work is the reproducibility of the anticipated peak structure. In Sec. III C, this issue is addressed by means of analyses of mock data generated from free spectral functions without peaks to see how reliably SpM reconstructs the spectral feature.

A. Mock spectral functions and correlation functions

Following Ref. [19] we consider the input spectral functions at temperatures below and above T_c

(i) For $T < T_c$

$$\hat{\rho}_{\mathrm{below}}(\hat{\omega}) = \tilde{\Theta}(\hat{\omega}, \hat{\omega}_1, \Delta_1)(1 - \tilde{\Theta}(\hat{\omega}, \hat{\omega}_2, \Delta_2))\hat{\rho}_{\mathrm{res}} + \tilde{\Theta}(\hat{\omega}, \hat{\omega}_3, \Delta_3)\hat{\rho}_{\mathrm{Wilson}} \tag{35}$$

(ii) For $T > T_c$

$$\hat{\rho}_{\mathrm{above}}(\hat{\omega}) = \hat{\rho}_{\mathrm{trans}} + \tilde{\Theta}(\hat{\omega}, \hat{\omega}_4, \Delta_4)(1 - \tilde{\Theta}(\hat{\omega}, \hat{\omega}_5, \Delta_5))\hat{\rho}_{\mathrm{res}} + \tilde{\Theta}(\hat{\omega}, \hat{\omega}_6, \Delta_6)\hat{\rho}_{\mathrm{Wilson}}. \tag{36}$$

Here $\hat{\rho}_{\mathrm{res}}$ denotes a resonance peak, $\hat{\rho}_{\mathrm{trans}}$ denotes a transport peak and $\hat{\rho}_{\mathrm{Wilson}}$ denotes a free Wilson spectral function [26,27] which takes the lattice cutoff effect into account. In Ref. [19] a free continuum spectral function is used in the $\hat{\rho}_{\mathrm{below}}$, but we use the free Wilson spectral function to account for the lattice cutoff effects even in the case of $T < T_c$.

The spectral functions are needed to be smooth, and the $\hat{\rho}_{\mathrm{res}}$, $\hat{\rho}_{\mathrm{trans}}$ and $\hat{\rho}_{\mathrm{Wilson}}$ that make up $\hat{\rho}_{\mathrm{below}}$ and $\hat{\rho}_{\mathrm{above}}$ are connected by a modified Θ function, which is given by

$$\tilde{\Theta}(\hat{\omega}, \hat{\omega}_i, \Delta_i) = \left(1 + \exp\left(\frac{\hat{\omega}_i^2 - \hat{\omega}^2}{\hat{\omega}\Delta_i}\right)\right)^{-1}. \tag{37}$$

The $\hat{\rho}_{\mathrm{res}}$, $\hat{\rho}_{\mathrm{trans}}$ and $\hat{\rho}_{\mathrm{Wilson}}$ are listed below

(i) Transport peak

$$\hat{\rho}_{\mathrm{trans}} = c_{\mathrm{trans}} \frac{\hat{\omega}\eta}{\hat{\omega}^2 + \eta^2}. \tag{38}$$

(ii) Resonance peak

$$\hat{\rho}_{\mathrm{res}} = c_{\mathrm{res}} \frac{\Gamma M \hat{\omega}^2}{(\hat{\omega}^2 - M^2)^2 + M^2\Gamma^2}. \tag{39}$$

(iii) Free Wilson spectral function

$$\hat{\rho}_{\mathrm{Wilson}} = c_{\mathrm{Wilson}} \frac{4\pi N_c}{N_\sigma^3} \sum_{\vec{k}} \sinh\left(\frac{\hat{\omega}}{2\hat{T}}\right) \times \left[b^{(1)} - b^{(2)} \frac{\sum_{i=1}^3 \sin^2 k_i}{\sinh^2 E_{\vec{k}}(m)}\right] \times \frac{\delta(\hat{\omega} - 2E_{\vec{k}}(m))}{2(1 + M_{\vec{k}}(m))^2 \cosh^2(\frac{E_{\vec{k}}(m)}{2\hat{T}})}, \tag{40}$$

where

$$\cosh E_{\vec{k}}(m) = 1 + \frac{K_{\vec{k}}^2 + M_{\vec{k}}^2(m)}{2(1 + M_{\vec{k}}(m))}, \tag{41}$$

$$K_{\vec{k}} = \sum_{i=1}^3 \gamma_i \sin k_i, \tag{42}$$

$$M_{\vec{k}}(m) = \sum_{i=1}^3 (1 - \cos k_i) + m. \tag{43}$$

The values of the parameters used in the above spectral function are summarized in Table I. These parameters mimic the physical situation at lattice spacing $a^{-1} = 20$ GeV, reflecting the fact that the position of the resonance peak is approximately J/ψ meson mass ($\sim$3.1 GeV) for $T < T_c$, and that a transport peak appears and the resonance peak becomes broader for $T > T_c$. In the free Wilson spectral function, the quark mass is set to be about 1.5 GeV, and the threshold of this spectral function can be adjusted by using the modified Θ function in the bound state region. The values of the parameters used in the Θ function are summarized in Table II.

The mock correlation function and the covariance matrix are obtained as follows. First, the correlation function is calculated by integrating the spectral function and the kernel K [see Eq. (27) or Eq. (30)]. Then, Gaussian random

TABLE I. Parameters for the mock spectral functions.

Spectral function	Parameters
$\hat{\rho}_{\mathrm{res}}$ for $\hat{\rho}_{\mathrm{below}}$	$c_{\mathrm{res}} = 0.08/7$, $\Gamma = 0.05$, $M = 0.155$
$\hat{\rho}_{\mathrm{Wilson}}$ for $\hat{\rho}_{\mathrm{below}}$	$c_{\mathrm{Wilson}} = 0.5$, $b^{(1)} = 2$, $b^{(2)} = 1$, $m = 0.073$, $N_c = 3$, $N_\sigma = 4096$
$\hat{\rho}_{\mathrm{trans}}$ for $\hat{\rho}_{\mathrm{above}}$	$c_{\mathrm{trans}} = 5 \times 10^{-5}$, $\eta = 0.006$
$\hat{\rho}_{\mathrm{res}}$ for $\hat{\rho}_{\mathrm{above}}$	$c_{\mathrm{res}} = 0.06$, $\Gamma = 0.15$, $M = 0.225$
$\hat{\rho}_{\mathrm{Wilson}}$ for $\hat{\rho}_{\mathrm{above}}$	$c_{\mathrm{Wilson}} = 1$, $b^{(1)} = 3$, $b^{(2)} = 1$, $m = 0.073$, $N_c = 3$, $N_\sigma = 4096$

TABLE II. Parameters for $\tilde{\Theta}$ functions.

$\hat{\omega}_1 = 0.145$	$\Delta_1 = 0.01$
$\hat{\omega}_2 = 0.155$	$\Delta_2 = 0.05$
$\hat{\omega}_3 = 0.225$	$\Delta_3 = 0.05$
$\hat{\omega}_4 = 0.225$	$\Delta_4 = 0.15$
$\hat{\omega}_5 = 0.225$	$\Delta_5 = 0.15$
$\hat{\omega}_6 = 0.350$	$\Delta_6 = 0.20$

numbers with standard deviation $\sigma_i = \varepsilon \cdot G(\tau_i) \cdot \tau_i$ are created at each Euclidean time. They correspond to the error with respect to the central value of the correlation function $G(\tau_i)$. In this study, we have 300 errors. These are added to the correlation function, and then 300 correlation functions $G^{(n)}(\tau_i)$ with errors, i.e., $N_{\mathrm{conf}} = 300$, are obtained. Using these correlation functions, we can calculate the covariance matrix C_{ij} by computing Eq. (18). In our mock-data tests, $\hat{\tau}_{\mathrm{r}}$ is set to 1, and also $\hat{\tau}_{\mathrm{min}}$ and $\hat{\tau}_{\mathrm{max}}$ are set to 1 and $N_\tau/2$, respectively.

B. Dependence on N_τ and noise level ε

To check the applicability of SpM to the number of input data and the magnitude of noise, we perform tests on three types of temporal extents, $N_\tau = 48$, 64 and 96, and three types of noise levels, $\varepsilon = 10^{-5}$, 5×10^{-3} and 10^{-2} in which $\varepsilon = 5 \times 10^{-3}$ is close to the quality of data of correlation functions calculated by using lattice QCD. Two types of kernels, $K_W^{(0)}(\hat{\tau}_i, \hat{\omega}_j)$ and $K_W^{(1)}(\hat{\tau}_i, \hat{\omega}_j)$, are used at temperature below T_{c}, and $K_W^{(0)}(\hat{\tau}_i, \hat{\omega}_j)$ is only used at temperature above T_{c} in the test. The parameters μ and μ' are introduced in the ADMM algorithm (see Appendix A in detail). We set $\mu = \mu' = 10^4$ for the test in which $K_W^{(0)}(\hat{\tau}_i, \hat{\omega}_j)$ is used and set $\mu = \mu' = 10^3$ for the test in which $K_W^{(1)}(\hat{\tau}_i, \hat{\omega}_j)$ is used (see Appendix E for information on how to determine μ and μ'). In all of the tests, the range of $\hat{\omega}$ of spectral functions is set from 0 to 4 and the number of points in ω-space is $N_\omega = 8001$. In the test for each combination of N_τ and ε, λ_{opt} is estimated between 3.5×10^2 and 6.6×10^4.

Figure 1 shows the spectral functions as a function of $\hat{\omega}$ for $T < T_{\mathrm{c}}$. These are obtained using $K_W^{(0)}(\hat{\tau}_i, \hat{\omega}_j)$, that is, $\hat{\rho}(\hat{\omega}_j)$ is obtained from $\tilde{\rho}^{(0)}(\hat{\omega}_j)$ calculated directly in ADMM. In Fig. 1(a), the results with a fixed noise level of $\varepsilon = 5 \times 10^{-3}$ for various N_τ are illustrated. The black solid line represents the input spectral function, and the blue dashed, green dotted and red dash-dotted lines represent the output results with $N_\tau = 48$, 64, and 96, respectively. It can be seen that the result for $N_\tau = 96$ has the sharpest peak and the position of the peak is closest to the input spectral function. Similar results are obtained for the other noise levels ε. This means that the more data points in the input correlation function, the better the reproducibility of the spectral function. In Fig. 1(b), the results with a fixed temporal extent of $N_\tau = 96$ for various ε are illustrated. The black solid line represents the input spectral function, and the blue dashed, green dotted, and red dash-dotted lines represent the output results with $\varepsilon = 10^{-2}$, 5×10^{-3} and 10^{-5}, respectively. It can be seen that the result for $\varepsilon = 10^{-5}$ has the sharpest peak and the position of the peak is closest to the input spectral function. Similar results are obtained for the other temporal extent N_τ. This means that the smaller the errors in the input correlation function, the higher the reproducibility.

In Fig. 1, the spectral function in the vicinity of $\hat{\omega} = 0$ exhibits a pronounced change in value, abruptly deviating to a positive or negative value. $\tilde{\rho}^{(0)}(\hat{\omega}_j)$ is directly obtained by using ADMM and $\hat{\rho}(\hat{\omega}_j)$ is calculated using Eq. (29). Therefore, $\hat{\rho}(\hat{\omega}_j)$ does not have to be a large positive or negative value for a small value of $\hat{\omega}$, reflecting the input spectral function and the positivity condition imposed on the spectral function in ADMM algorithm. However, the magnitude of $\hat{\rho}(\hat{\omega}_j)/\hat{\omega}^2$ becomes large since $\hat{\rho}(\hat{\omega}_j)$ is

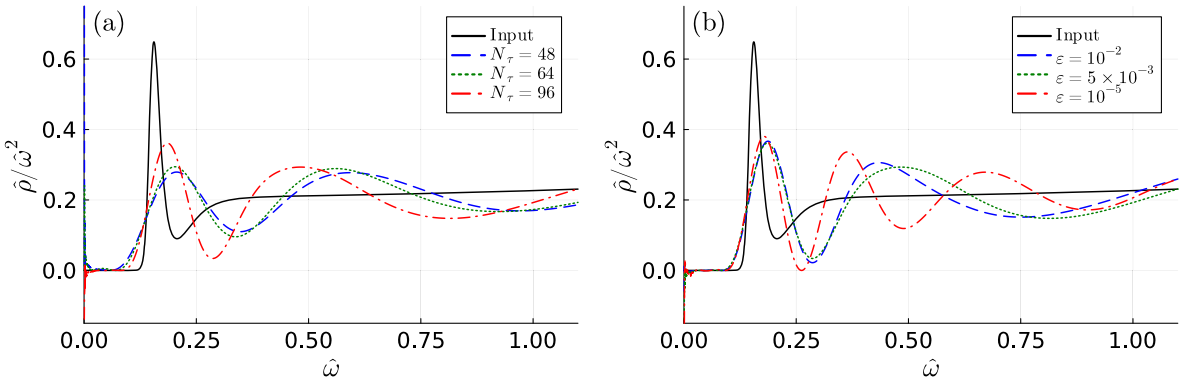

FIG. 1. Spectral functions obtained by using $K_W^{(0)}(\hat{\tau}_i, \hat{\omega}_j)$ in the mock-data tests for $T < T_{\mathrm{c}}$. Figure (a) shows the results with a fixed noise level of $\varepsilon = 5 \times 10^{-3}$. The blue dashed, green dotted, and red dash-dotted lines represent the output results with $N_\tau = 48$, 64 and 96, respectively. Figure (b) shows the results with a fixed temporal extent of $N_\tau = 96$. The blue dashed, green dotted, and red dash-dotted lines represent the output results with $\varepsilon = 10^{-2}$, 5×10^{-3} and 10^{-5}, respectively. In both figures, the black solid line represents the input spectral function.

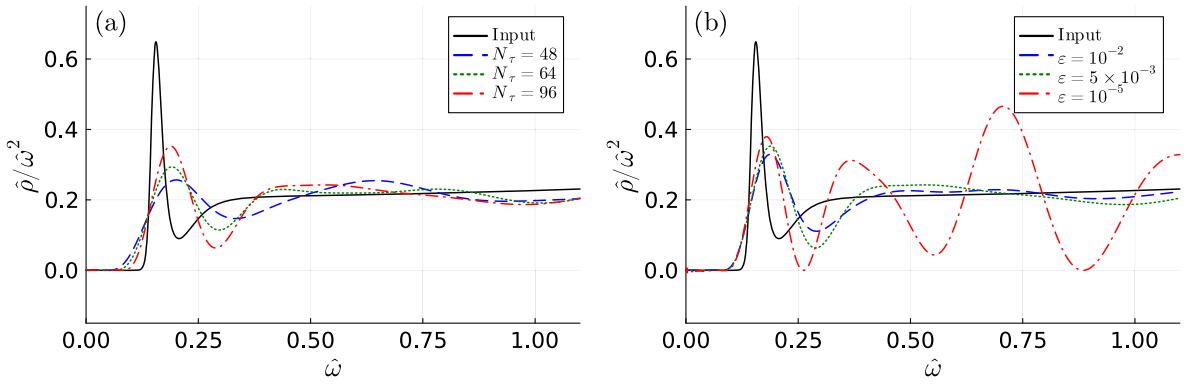

FIG. 2. Same as Fig. 1 but obtained by using $K_W^{(1)}(\hat{\tau}_i, \hat{\omega}_j)$. Figures (a) and (b) show the results with $\varepsilon = 5 \times 10^{-3}$ and $N_\tau = 96$, respectively.

divided by the square of a small value of $\hat{\omega}$. Thus, what appears to be a peak in the vicinity of $\hat{\omega} = 0$ is, in fact, a fake.

Figure 2 shows the same results as in Fig. 1 but obtained by using $K_W^{(1)}(\hat{\tau}_i, \hat{\omega}_j)$, that is, $\hat{\rho}(\hat{\omega}_j)$ are obtained from $\tilde{\rho}^{(1)}(\hat{\omega}_j)$ calculated directly in ADMM. From Fig. 2(a), increasing N_τ results in better spectral functions that are closer to the input spectral function. Similar results are obtained for the other noise levels ε. From Fig. 2(b), reducing ε results in better spectral functions that are closer to the input spectral function. Similar results are obtained for the other temporal extents N_τ.

In contrast to the results of the spectral functions with $K_W^{(0)}(\hat{\tau}_i, \hat{\omega}_j)$ shown in Fig. 1, the values of the spectral function in the vicinity of $\hat{\omega} = 0$ are not large. As mentioned in Sec. II C, $\tilde{\rho}^{(1)}(0) = 0$ is implicitly imposed, that is, $\hat{\rho}(0) = 0$ is ensured. Thus, there would be no fake peak.

Figure 3 shows the same results as in Fig. 1, but for $T > T_c$. From Fig. 3(a), it can be seen that the result for $N_\tau = 96$ has the closest resonance peak to the input spectral function. Similar results are obtained for the other noise levels ε. This means that the more data points in the input correlation function, the better the reproducibility of the spectral function. From Fig. 3(b), it can be seen that the result for $\varepsilon = 10^{-5}$ has the closest resonance peak to the input spectral function. Similar results are obtained for the other temporal extent N_τ. This means that the smaller the errors in the input correlation function, the higher the reproducibility.

The change in value of the spectral function shown in Fig. 3 is more gradual than for $T < T_c$ shown in Fig. 1. In the case of $N_\tau = 64$ shown in Fig. 3(a) and that of $\varepsilon = 10^{-5}$ shown in Fig. 3(b), these appear to fit well with the transport peak of the input spectral function. In order to confirm this, we illustrate $\hat{\rho}/(\hat{\omega}\hat{T})$ as a function of $\hat{\omega}$ in Fig. 4, which is an enlarged view of the plot in Fig. 3(b) at small $\hat{\omega}$. Note that $\hat{T} = N_\tau^{-1}$. The values of the spectral function in this region are nonzero, which may reflect the transport peak in the input spectral function. On the other hand, the value of the spectral function in the limit of $\hat{\omega} \to 0$ for $\varepsilon = 5 \times 10^{-3}$ is closest to that of the input spectral function. This does not mean that the smaller the error, the better the reproducibility, as is the case with the resonance peak. Even when other combinations of N_τ and ε are examined, it cannot be concluded that a smaller error necessarily leads to better reproducibility of the value of the spectral function in the limit of $\hat{\omega} \to 0$, nor that increasing N_τ improves the reproducibility in the same limit.

The results for $T > T_c$ shown in Fig. 3 indicate that some of the input and output resonance peaks are relatively well matched, whereas the results for $T < T_c$ shown in Figs. 1 and 2 indicate that they are not well matched to the sharp peaks in the input spectral function. The transport peak mentioned above is also accompanied by an abrupt change in value. These results suggest that sparse solutions of spectral functions in the IR basis may not adequately represent the abrupt change in value of the spectral function in the original basis.

In regions where $\hat{\omega} \gtrapprox 0.30$, the output spectral function has wavy results. In particular, spectral functions with larger amplitudes tend to be obtained when the noise level ε is small. It can be seen that these results show the overfitting behavior for the spectral function in the regions. It is shown in [20] that SpM with weak regularization ($\lambda < \lambda_{\text{opt}}$) results in overfitting. Although λ_{opt} is decided following the previous study, it appears that when the error in the correlation function is small and the spectral function has a sharp peak structure, λ_{opt} is chosen, which is overfitting for the spectral function in the regions. On the basis of the above discussion, an additional assumption beyond sparseness may be needed for extracting a spectral function with an abrupt change in value.

We also conduct several tests using mock data of spectral functions with two resonance peaks in the low-frequency region. The results confirm that only the output of the first peak is valid, and that the positions of the second and subsequent peaks cannot be determined. Furthermore, when the mock spectral function has two sharp peaks within a narrow frequency range, the peak obtained by SpM in that

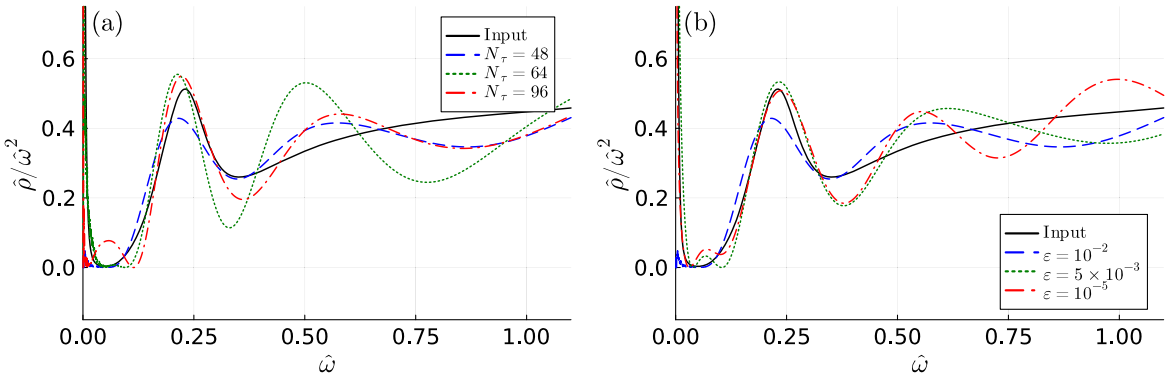

FIG. 3. Same as Fig. 1 but for $T > T_c$. Figures (a) and (b) show the results with $\varepsilon = 10^{-2}$ and $N_\tau = 48$, respectively.

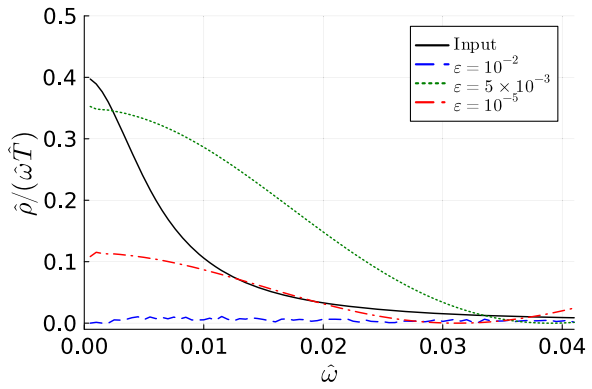

FIG. 4. $\hat{\rho}/(\hat{\omega}\hat{T})$ as a function of $\hat{\omega}$, which is an enlarged view of the plot in Fig. 3(b) in the very small value of $\hat{\omega}$. Note that $\hat{T} = N_\tau^{-1}$.

frequency range appears as a single broad peak. As mentioned in Sec. II C section, SpM preferentially reconstructs spectral functions with moderate width, as sharply localized peaks typically involve contributions from high-frequency modes that are poorly constrained by the Euclidean correlator data. As a result, reconstructions based solely on the sparsity assumption tend to yield spectral functions with a resolution limited by the information content of the data.

C. Validation using free spectral functions

In order to further assess the reliability of the spectral functions reconstructed by SpM, as discussed in the previous section, we conduct additional tests using mock spectral functions that contain no peaks. We have extracted spectral functions by using SpM from correlation functions made from mock spectral functions with no peaks, and the results of the output spectral function match the input spectral function well [28]. However, since the settings considered in [28] differ from those in this study, it is meaningful to revisit investigations using spectral functions without peaks.

The input spectral functions without peaks at temperatures below and above T_c are prepared based on the mock spectral functions introduced in Sec. III A. For temperatures below T_c, we use the spectral function with $c_{\mathrm{res}} = 0$, consisting solely of the free Wilson spectral function and the modified Θ function. For temperatures above T_c, we adopt the spectral function with $c_{\mathrm{res}} = c_{\mathrm{trans}} = 0$, again consisting only of the free Wilson spectral function and the

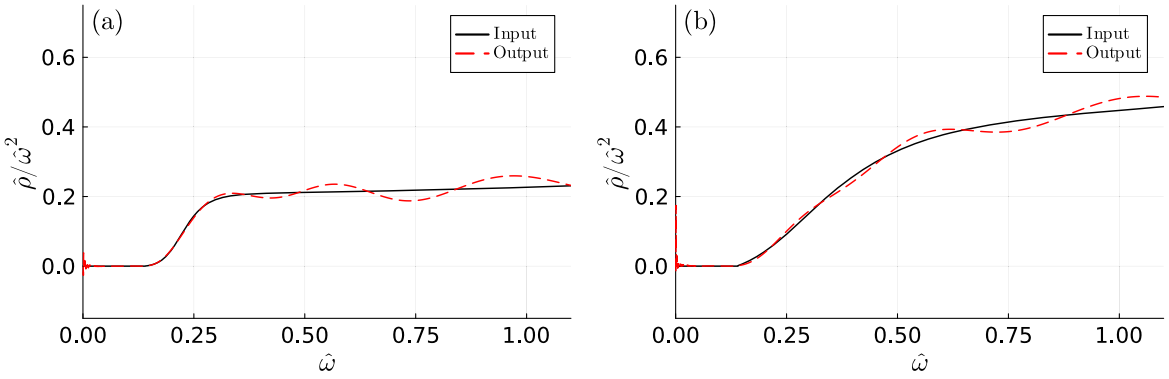

FIG. 5. Spectral functions reconstructed from correlation functions calculated using the mock free spectral function. Figure (a) shows the results with $K_W^{(0)}(\hat{\tau}_i, \hat{\omega}_j)$, $N_\tau = 96$ and a noise level of $\varepsilon = 10^{-5}$ for $T < T_c$. Figure (b) shows the results with $K_W^{(0)}(\hat{\tau}_i, \hat{\omega}_j)$, $N_\tau = 48$ and a noise level of $\varepsilon = 10^{-5}$ for $T > T_c$. In both figures, the black solid and the red dashed lines represent the input and the output spectral function, respectively.

modified Θ function. Note that all other settings—such as N_τ, ε, μ, and μ'—are kept identical to those used in the previous section.

Figure 5 shows our typical results of the spectral functions. In Fig. 5(a), the red dashed line represents the output result with $N_\tau = 96$ and $\varepsilon = 10^{-5}$ for $T < T_c$, and the black solid line represents the input spectral function. In Fig. 5(b), the red dashed line represents the output result with $N_\tau = 48$ and $\varepsilon = 10^{-5}$ for $T > T_c$, and the black solid line represents the input spectral function. The output results at both temperatures show good agreement with their respective inputs. Similar results are obtained across various combinations of N_τ and ε. Furthermore, note that the results were obtained by using $K_W^{(0)}(\hat{\tau}_i, \hat{\omega}_j)$, and we confirm that results of comparable quality are also obtained when using $K_W^{(1)}(\hat{\tau}_i, \hat{\omega}_j)$.

The input free spectral function exhibits different frequency dependences below and above T_c, yet SpM reconstructs these behaviors successfully. The results presented in Sec. III B demonstrate that the output of SpM reflects the increase in values due to the presence of resonance peaks in the spectral function. Conversely, when the input correlation function lacks information of a resonance peak, SpM does not generate spurious peak structures.

IV. RESULTS FROM LATTICE QCD DATA

In this section we show results of the charmonium spectral function in pseudoscalar and vector channels extracted from the correlation functions calculated by using lattice QCD. These lattice data used in this study were given in ref. [29], where the correlation functions were measured with the $O(a)$-improved Wilson quark action on quenched gauge configurations generated by using the standard plaquette gauge action. The lattice spacing $a = 0.010$ fm and the corresponding a^{-1} is about 18.97 GeV. The spatial extent N_σ is 128, and the temporal extent N_τ is 48 and 96. These setup correspond to temperature $T \simeq 0.73T_c$ and $1.46T_c$. The number of gauge configurations is 234 for $T \simeq 0.73T_c$ and 461 for $T \simeq 1.46T_c$. We utilized meson correlation functions in the pseudoscalar and the vector channels for each temperature. We set $\hat{\tau}_r = 4$, and use the data of the correlation function from $\hat{\tau}_r$ to $N_\tau/2$.

As in the case of mock-data tests, two types of kernel written in Eq. (33) are considered in our calculations, that is, $K_W^{(0)}(\hat{\tau}_i, \hat{\omega}_j)$ and $K_W^{(1)}(\hat{\tau}_i, \hat{\omega}_j)$ are used for $T \simeq 0.73T_c$, and only $K_W^{(0)}(\hat{\tau}_i, \hat{\omega}_j)$ is used for $T \simeq 1.46T_c$. We also set the range of $\hat{\omega}$ of the spectral functions from 0 to 4, and the number of points in ω-space to $N_\omega = 8001$. In the analyses using actual lattice QCD data, $\lambda_{\rm opt}$ is estimated between 4.0×10^3 and 3.1×10^5. The values of the parameters μ and μ' are set $\mu = \mu' = 10^2$, 10^3 and 10^4 (see Appendix E for information on how to determine μ and μ'). The statistical error of the spectral function is estimated using the jackknife method with a bin size of one.

Figure 6 shows our typical results of the spectral functions in (a) vector and (b) pseudoscalar channels for $T \simeq 0.73T_c$. These are obtained using $K_W^{(0)}(\hat{\tau}_i, \hat{\omega}_j)$, that is, $\hat{\rho}(\hat{\omega}_j)$ is obtained from $\tilde{\rho}^{(0)}(\hat{\omega}_j)$ calculated directly in ADMM, and the parameters μ and μ' in ADMM algorithm are set to 10^2. The blue shaded areas represent the statistical errors of the spectral functions from jackknife analyses, the blue solid lines represent the mean values, and the black horizontal error bars at the top of the first peaks represent the uncertainty of the location of the resonance peak for each spectral function. The value of the spectral function increases around 2 GeV, and the average value of the location of the first peak is about 4 GeV in both channels. Similar results are obtained for $\mu = \mu' = 10^3$ and 10^4. The mean values, statistical errors, and systematic errors of the location of the resonance peak, which are estimated after considering all values of μ, are listed in Table III. The mean values are 4.02 GeV in the pseudoscalar channel and 4.30 GeV in the vector channel, while those obtained from MEM are 3.31 GeV in the pseudoscalar channel and 3.48 GeV in the vector channel [29]. Although our result is somewhat larger than that of the previous study, the

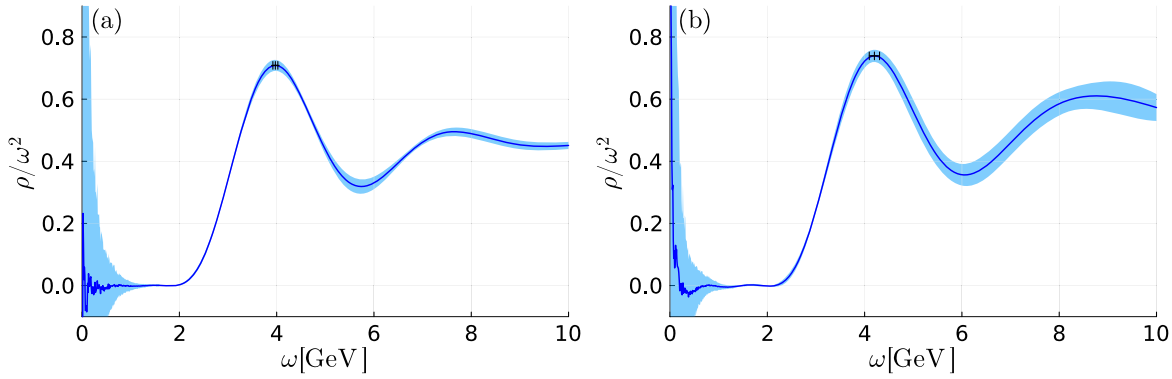

FIG. 6. Spectral functions obtained by using $K_W^{(0)}(\hat{\tau}_i, \hat{\omega}_j)$ in (a) pseudoscalar and (b) vector channels extracted from actual lattice QCD data for $T \simeq 0.73T_c$. The parameters μ and μ' in ADMM algorithm are set to 10^2. The blue shaded areas represent the statistical errors of the spectral functions from jackknife analyses, the blue solid lines represent the mean values, and the black horizontal error bars represent the uncertainty of the location of the first peak for each spectral function.

TABLE III. The mean values, statistical errors, and systematic errors of the location of the resonance peak. The "PS" and the "VC" stand for pseudoscalar and vector channel, respectively. The "stat." stands for statistical errors estimated by jackknife method and the "sys." stands for systematic errors from SpM analyses in Appendix E.

T/T_c	Channel	Kernel $K_W^{(n)}$	Resonance peak
0.73	PS	$n=0$	$4.02 \pm 0.08(\text{stat})^{+0.04}_{-0.05}(\text{sys})$
		$n=1$	$4.07 \pm 0.06(\text{stat})^{+0.06}_{-0.06}(\text{sys})$
	VC	$n=0$	$4.30 \pm 0.09(\text{stat})^{+0.07}_{-0.10}(\text{sys})$
		$n=1$	$4.27 \pm 0.07(\text{stat})^{+0.08}_{-0.05}(\text{sys})$
1.46	PS	$n=0$	$4.87 \pm 0.08(\text{stat})^{+0.01}_{-0.01}(\text{sys})$
	VC	$n=0$	$5.42 \pm 0.16(\text{stat})^{+0.00}_{-0.01}(\text{sys})$

qualitative behavior is consistent: a well-defined resonance peak is observed, with its position in the pseudoscalar channel appearing at a lower frequency than in the vector channel.

Focusing on the very low frequency of the spectral function shown in Fig. 6, we can see that it slightly fluctuates around $\rho = 0$ in the pseudoscalar channel or rapidly increases in value in the vector channel. It is similar to the spectral functions obtained using $K_W^{(0)}(\hat{\tau}_i, \hat{\omega}_j)$ in the mock-data tests. Since $\hat{\rho}(\hat{\omega}_j)$ is calculated using Eq. (29), $\rho(\omega)$ does not have to be a large magnitude for a small value of ω. Since $\rho(\omega)$ is divided by the square of a small value of ω, however, the magnitude of $\rho(\omega)/\omega^2$ becomes large. The statistical errors represented by the blue shaded areas are also very large. This means that the spectral function at low frequencies calculated using $K_W^{(0)}(\hat{\tau}_i, \hat{\omega}_j)$ has large differences for each jackknife sample and its value is not settled. At a temperature below T_c, $\rho = 0$ is expected in the limit of $\omega \to 0$, i.e., it may be better not to use $K_W^{(0)}(\hat{\tau}_i, \hat{\omega}_j)$ in calculations at a temperature below T_c.

Figure 7 shows the same results as in Fig. 6 but obtained using $K_W^{(1)}(\hat{\tau}_i, \hat{\omega}_j)$. The results are similar to those obtained using $K_W^{(0)}(\hat{\tau}_i, \hat{\omega}_j)$, and similar results are obtained for $\mu = \mu' = 10^3$ and 10^4. As shown in the values of the resonance peak listed in Table III, the position of the resonance peak from $\tilde{\rho}^{(0)}(\hat{\omega}_j)$ is almost the same as that from $\tilde{\rho}^{(1)}(\hat{\omega}_j)$. Therefore, the qualitative behavior remains consistent with the previous study [29]. This common behavior strongly suggests that it reflects the underlying physics of the charmonium spectral function.

In contrast to the results of the spectral functions with $K_W^{(0)}(\hat{\tau}_i, \hat{\omega}_j)$ shown in Fig. 6, the average values of the spectral function in the low-ω region are flat at $\rho = 0$. It is similar to the spectral functions obtained using $K_W^{(1)}(\hat{\tau}_i, \hat{\omega}_j)$ in the mock-data tests. Since $\hat{\rho}(0) = 0$ is implicitly imposed, $\rho(0) = 0$ is ensured. In addition, the statistical errors of the spectral function in the low-ω region are very small. This means that the spectral function in low-ω region calculated using $K_W^{(1)}(\hat{\tau}_i, \hat{\omega}_j)$ differs little for each jackknife sample. Therefore, SpM analysis using $K_W^{(1)}(\hat{\tau}_i, \hat{\omega}_j)$ gives a stable solution.

Figure 8 shows the same results as in Fig. 6 but for $T \simeq 1.46 T_c$. Compared to the results for $T \simeq 0.73 T_c$, the peaks are broader and located at higher energies, and similar results are obtained for $\mu = \mu' = 10^2$ and 10^4. As shown in the values of the resonance peak listed in Table III, the average values of the location of the resonance peak are 4.87 GeV in the pseudoscalar channel and 5.42 GeV in the vector channel. These values are also larger than the results of the previous study [29] in which the results obtained from MEM are about 4.1 GeV in the pseudoscalar channel and about 4.7 GeV in the vector channel. However, the qualitative behavior remains consistent, having a broad peak with its location in the pseudoscalar channel appearing at a lower frequency than in the vector channel. Although systematic errors were not estimated using the same method as in the previous study, it seems that, based on the peak width and qualitative consistency with the previous study, it is possible to conclude that the η_c corresponding to the pseudoscalar

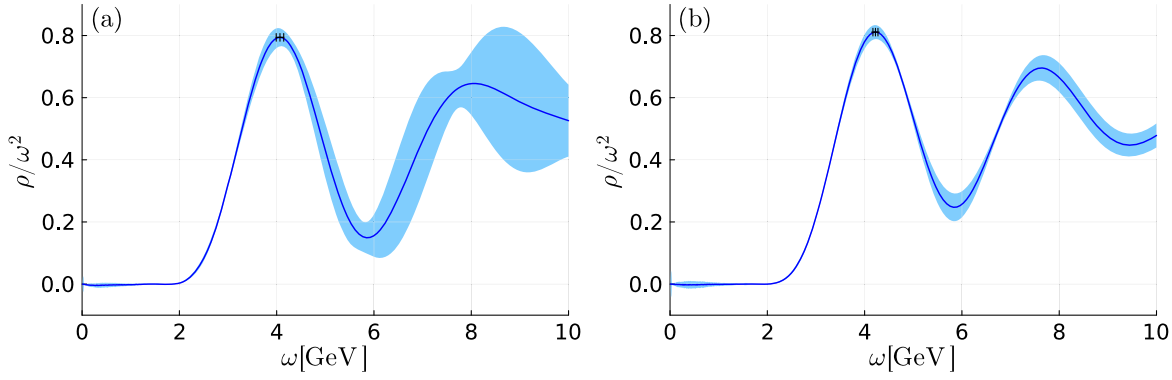

FIG. 7. Same as Fig. 6 but obtained by using $K_W^{(1)}(\hat{\tau}_i, \hat{\omega}_j)$. Figures (a) and (b) show the results with pseudoscalar and vector channels, respectively. The parameters μ and μ' in ADMM algorithm are set to 10^2.

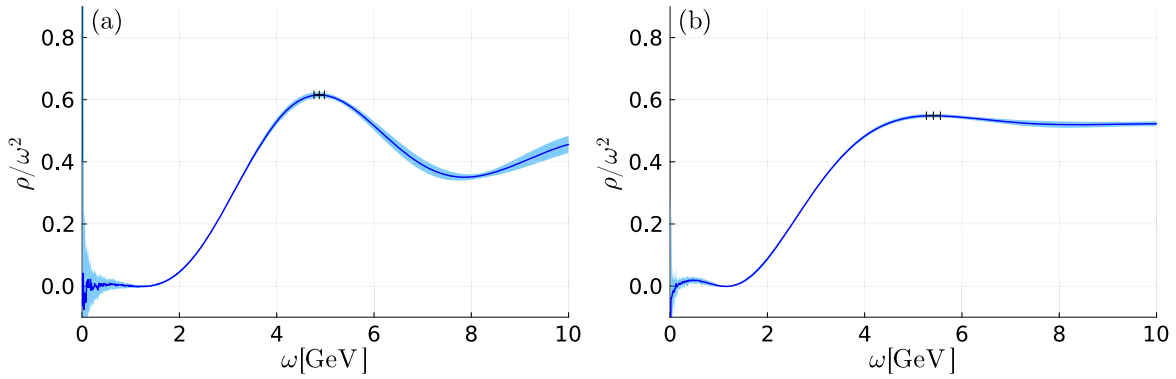

FIG. 8. Same as Fig. 6 but for $T \simeq 1.46 T_c$. Figures (a) and (b) show the results in pseudoscalar and vector channels, respectively. The parameters μ and μ' in ADMM algorithm are set to 10^2.

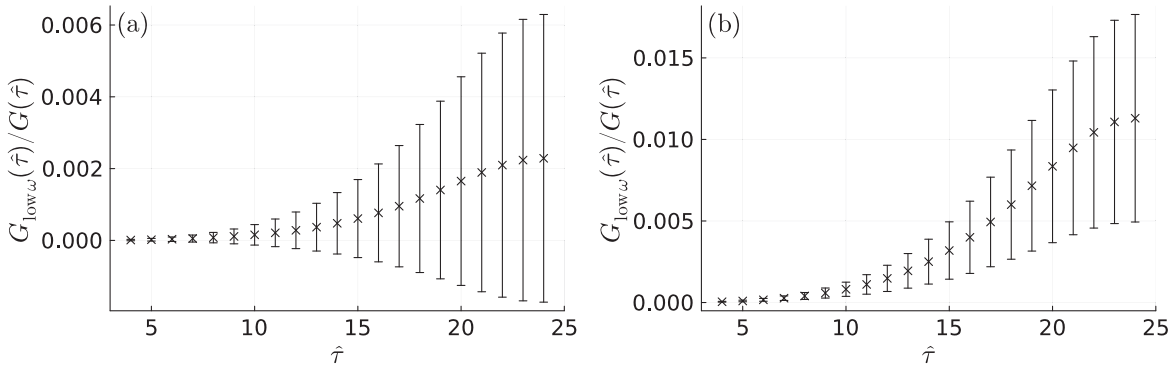

FIG. 9. Ratios $G_{\mathrm{low}\omega}(\hat{\tau})/G(\hat{\tau})$ of correlation functions calculated using the spectral functions shown in Fig. 8, where $G_{\mathrm{low}\omega}(\hat{\tau})$ is evaluated using the spectral function up to a frequency of 1.5 GeV and $G(\hat{\tau})$ over the entire frequency range. Figures (a) and (b) show the results in pseudoscalar and vector channels, respectively. The crosses denote the mean values of the ratios, and the vertical error bars represent the statistical errors of the ratios from jackknife analyses.

channel and the J/ψ corresponding to the vector channel are already melted at $1.46\,T_c$.

In low frequency region, the value of the spectral function slightly fluctuates around $\rho = 0$ and the statistical error of the spectral function in the vicinity of $\omega = 0$ is very large in the pseudoscalar channel in Fig. 8(a). These behaviors are similar to those for $T < T_c$ shown in Fig. 6(a). If these fluctuations in low-frequency region were meaningful, they should contribute to the correlation function. In order to examine these contributions, we calculate the correlation function using the spectral function up to a frequency of 1.5 GeV. Figure 9(a) shows the ratio $G_{\mathrm{low}\omega}(\hat{\tau})/G(\hat{\tau})$ of correlation functions calculated using the spectral functions shown in Fig. 8(a), where $G_{\mathrm{low}\omega}(\hat{\tau})$ is evaluated using the spectral function up to a frequency of 1.5 GeV and $G(\hat{\tau})$ is evaluated over the entire frequency range. The crosses denote the mean values of the ratios, and the vertical error bars represent the statistical errors of the ratios from jackknife analyses. The results show it to be zero within the error range. This finding suggests the absence of a transport peak.

In the vector channel at $T > T_c$, although it is expected that the presence of the transport peak will be extracted, in our analyses, it does not appear as shown in Fig. 8(b). Furthermore, the values of the spectral function in the vicinity of $\omega = 0$ GeV are negative, despite applying the constraint of positivity of the spectral function. We confirm that the positivity is rendered more protected as μ and μ' increase, and the values of the spectral function in the vicinity of $\omega = 0$ GeV approach zero, but do not turn to large positive values such as the transport peak. In contrast to the pseudoscalar channel, however, the statistical error of the spectral function in the low-frequency region is small. Therefore, the possibility of signal existence is considered. As with the pseudoscalar channel, we calculate the correlation function using the spectral function up to a frequency of 1.5 GeV in order to examine its contribution to the correlation function. Figure 9(b) shows the same result in Fig. 9(a) but for the vector channel. This result indicates that, in contrast to the case of pseudoscalar channel, there is a statistically significant contribution. This means that, as seen in the mock-data test, the contribution below the threshold appears to exist in the presence of the transport

peak, suggesting that some signal may indeed be present. In order to estimate the transport with reasonable accuracy, it may be necessary to make additional assumptions that extend beyond SpM, including the shape of the transport peak.

V. SUMMARY

We applied SpM to extract a spectral function from a Euclidean-time meson correlation function. SpM is a method that solves inverse problems by considering only the sparseness of the solution we seek. Since the correlation function has correlation between different Euclidean times, we took the covariance of the correlation function into account for SpM.

First, we tested SpM with mock data of the spectral function. In order to check the applicability of SpM for the number of data points of the correlation function and the magnitude of errors of the correlation function, we used the possible charmonium spectral function for $T < T_c$ and $T > T_c$. To examine whether the anticipated peak structure can be reproduced only when it is genuinely present, we also considered a free spectral function in which resonance peaks are intentionally absent. This method was found to be poor at precisely reconstructing spectral functions with abrupt changes in value, such as sharp peaks at $T < T_c$ and transport peaks at $T > T_c$. However, this test confirmed that increasing the number of data points of the correlation function and reducing the magnitude of errors of the correlation function lead to output spectral functions closer to the input spectral function and, when the input correlation function lacks information of a resonance peak, this method does not generate spurious peak structures.

Next, we tried to extract the spectral functions from the charmonium correlation functions in pseudoscalar and vector channels at $T \simeq 0.73T_c$ with $N_\tau = 96$ and $T \simeq 1.46T_c$ with $N_\tau = 48$ obtained by lattice QCD. We got a spectral function with a broad peak around 4 GeV in each channel for $T < T_c$, which is slightly larger compared to the results in the previous study using MEM [29]. For $T \simeq 1.46T_c$, compared to the results for $T \simeq 0.73T_c$, we got a spectral function with a broader peak around 5 GeV in each channel, which is also larger compared to the results from MEM. In addition, our calculation does not yield the transport peak, which is expected to be the presence in the vector channel. In order to estimate the transport peak, it may be necessary to make assumptions that extend beyond the sparse modeling, including the shape of the transport peak. Although the positions and the widths of the resonance peak differ from the results from MEM as described above, the qualitative behavior is the same; there is a physically consistent hierarchy in peak positions across channels, and a clearly defined peak appears at lower temperatures that broadens at higher temperatures. Therefore, this result, solely from the assumption of the sparse solution, reflects underlying physics.

ACKNOWLEDGMENTS

Our SpM analyses were performed using code created by E. Itou and Y. Nagai. We are grateful to H.-T. Ding for sharing lattice data, and to E. Itou and Y. Nagai for fruitful discussions at an early stage of this work. The work of A. T. was partially supported by JSPS KAKENHI Grant No. 20K14479, 22H05111, 22K03539, and 25K07287 and JST BOOST, Japan Grant No. JPMJBY24F1. A. T. and H. O. were partially supported by JSPS KAKENHI Grant No. 22H05112. This work was partially supported by MEXT as "Program for Promoting Researches on the Supercomputer Fugaku" (Grant No. JPMXP1020230411 and JPMXP1020230409).

DATA AVAILABILITY

The data that support the findings of this article are not publicly available upon publication because it is not technically feasible and/or the cost of preparing, depositing, and hosting the data would be prohibitive within the terms of this research project. The data are available from the authors upon reasonable request.

APPENDIX A: ADMM ALGORITHM

In this appendix, we briefly review the ADMM algorithm following Refs. [22,23]. This algorithm, which is developed by Ref. [25], solves the optimization problem that includes an L_1 regularization term with multiple constraints.

We need to find a minimization of $F(\vec{\rho}'_W|\vec{G}'_W, \lambda)$ in Eq. (26) with respect to $\vec{\rho}'_W$ with two additional constraints in Eqs. (15) and (16). Following the conventional notation, we change the variables as $\vec{\rho} \to \vec{x}$, $\vec{\rho}'_W \to \vec{x}'$, $\vec{G}_W \to \vec{y}$, and $\vec{G}'_W \to \vec{y}'$, and the matrix as $S_W \to S$. Then the cost function is rewritten as

$$F(\vec{x}'|\vec{y}', \lambda) = \frac{1}{2}\|\vec{y}' - S\vec{x}'\|_2^2 + \lambda\|\vec{x}'\|_1, \tag{A1}$$

and the constraints are represented as

$$x_j \geq 0, \qquad \sum_j x_j = 1. \tag{A2}$$

The dimension of this optimization problem is given by $L = \min(M, N)$, where M and N are the sizes of $\vec{y}$ and $\vec{x}$, respectively. In fact, we can reduce L by introducing a cut of the singular value in analysis, and we mentioned the method of reducing the dimension in Sec. II D.

In the ADMM algorithm, we introduce auxiliary vectors $\vec{z}$ and $\vec{z}'$, and consider minimization of the function

$$\tilde{F}(\vec{x}', \vec{z}', \vec{z}) = \frac{1}{2\lambda}\|\vec{y}' - S\vec{x}'\|_2^2 - \nu(\langle V\vec{x}'\rangle - 1) + \|\vec{z}'\|_1 + \lim_{\gamma\to\infty}\gamma\sum_j \Theta(-z_j), \tag{A3}$$

subject to

$$\vec{z}' = \vec{x}', \qquad \vec{z} = V\vec{x}', \tag{A4}$$

where we have used a convention that primed vectors denote quantities represented in the IR basis, V is the matrix obtained by the SVD, $\langle V\vec{x}'\rangle$ represents the sum of the components of $V\vec{x}'$, and Θ is the Heaviside step function. The sum rule is imposed by the Lagrange multiplier ν, and non-negativity is expressed by an infinite potential with γ. The auxiliary vectors $\vec{z}$ and $\vec{z}'$ are in charge of the L_1 regularization and the non-negativity, respectively.

The constraints for the auxiliary vectors, which are given in Eq. (A4), are treated by the augmented Lagrange multiplier method. In order to treat the first constraint, $\vec{z}' = \vec{x}'$, normalized Lagrange multipliers $\vec{u}'$ and a parameter μ' are introduced. Similarly, in order to treat the second constraint, $\vec{z} = V\vec{x}'$, normalized Lagrange multipliers $\vec{u}$ and a parameter μ are introduced. With the introduction of $\vec{u}$, $\vec{u}'$, μ, and μ', the loss function actually applied to the ADMM algorithm is expressed as

$$\begin{aligned}\tilde{L}_{\mathrm{aug}} = &\frac{1}{2\lambda}\|\vec{y}' - S\vec{x}'\|_2^2 + \|\vec{z}'\|_1 \\ &+ \frac{\mu'}{2}\|\vec{x}' - \vec{z}' + \vec{u}'\|_2^2 - \frac{\mu'}{2}\|\vec{u}'\|_2^2 \\ &+ \frac{\mu}{2}||V\vec{x}' - \vec{z} + \vec{u}||_2^2 - \frac{\mu}{2}||\vec{u}||_2^2 \\ &- \nu(\langle V\vec{x}'\rangle - 1) + \lim_{\gamma\to\infty}\gamma\sum_j \Theta(-z_j).\end{aligned} \tag{A5}$$

While $\vec{u}$ and $\vec{u}'$ are iteratively updated together with its conjugate vectors $\vec{z}$ and $\vec{z}'$, respectively, the coefficients μ and μ' are predetermined. In addition, μ and μ' control speed of convergence.

Considering the search for the minimum value of the loss function $\tilde{L}_{\mathrm{aug}}$., we obtain update formulas used in actual computations

$$\begin{aligned}\vec{x}' \leftarrow &\left(\frac{1}{\lambda}S^{\mathrm{t}}S + (\mu' + \mu)I\right)^{-1} \\ &\times \left(\frac{1}{\lambda}S^{\mathrm{t}}\vec{y}' + \mu'(\vec{z}' - \vec{u}') + \mu V^{\mathrm{t}}(\vec{z} - \vec{u}) + \nu V^{\mathrm{t}}\vec{e}\right) \\ &\equiv \vec{\xi}_1 + \nu\vec{\xi}_2,\end{aligned} \tag{A6}$$

$$\vec{z}' \leftarrow \mathcal{S}_{1/\mu'}(\vec{x}' + \vec{u}'), \tag{A7}$$

$$\vec{u}' \leftarrow \vec{u}' + \vec{x}' - \vec{z}', \tag{A8}$$

$$\vec{z} \leftarrow \mathcal{P}_+(V\vec{x}' + \vec{u}), \tag{A9}$$

$$\vec{u} \leftarrow \vec{u} + V\vec{x}' - \vec{z}, \tag{A10}$$

where I is the unit matrix, $e_i = 1$,

$$\nu = \frac{1 - \langle V\vec{\xi}_1\rangle}{\langle V\vec{\xi}_2\rangle}. \tag{A11}$$

Here, $\mathcal{P}_+$ denotes a projection operator onto non-negative quadrant, i.e., $\mathcal{P}_+(z_j) = \max(z_j, 0)$ for each element, and $\mathcal{S}_\alpha$ denotes the element-wise soft thresholding function, which is defined for each element by

$$\mathcal{S}_\alpha(x) = \begin{cases} x - \alpha & (x > \alpha) \\ 0 & (-\alpha \le x \le \alpha) \\ x + \alpha & (x < -\alpha) \end{cases}. \tag{A12}$$

The updates in Eqs. (A6)–(A10) are iteratively performed until convergence is reached.

In our SpM analyses, whether convergence has been achieved is determined by looking at the value of the residuals, $\|\vec{z} - V\vec{x}'\|_1/N_\omega$. Also, ν is set to zero since the condition of the sum rule is not applied, the initial vectors are set at zero vectors for all and we set the coefficients μ and μ' at 10^2–10^4. The actual values of μ and μ' are written in Secs. III and IV, and we explain how to determine these values of μ and μ' in Appendix E.

APPENDIX B: SINGULAR VALUES OF THE KERNEL K_W

One of the key to solving the inverse problem by SpM is dimensionality reduction. In order to utilize this reduction, it is necessary that the components of the singular values of the kernel decrease exponentially. In previous studies [20,22], kernels of the type given by Eq. (2) have been used, and their singular values have been shown to decrease exponentially. On the other hand, our study employs the kernel $K_W^{(n)}$ defined by Eq. (33). The singular value of this kernel must be investigated.

Figure 10 shows the singular values of the kernel $K_W^{(0)}$ given in Eqs. (28) and (33) with $N_\tau = 96$ and $\varepsilon = 5 \times 10^{-3}$. The singular values decrease exponentially, indicating that dimensionality reduction can be used. It has also been made

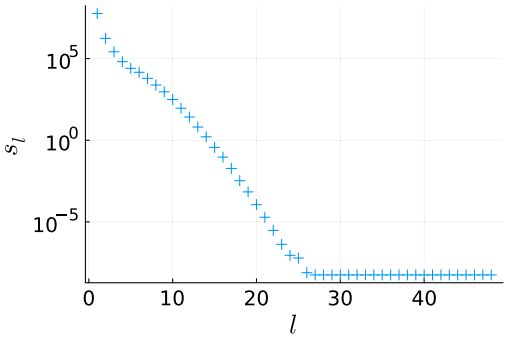

FIG. 10. Singular values of the kernel $K_W^{(0)}$ with $N_\tau = 96$ and $\varepsilon = 5 \times 10^{-3}$.

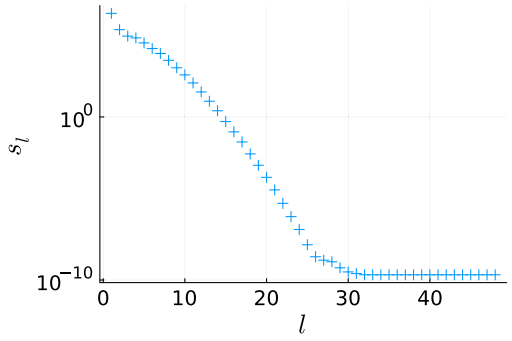

FIG. 11. Same as Fig. 10 but for the kernel $K_W^{(1)}$.

sure that the singular values of the kernel $K_W^{(0)}$ decrease exponentially for other combinations of N_τ and ε as well.

Figure 11 shows the same as in Fig. 10 but for the kernel $K_W^{(1)}$ given in Eqs. (31) and (33) with $N_\tau = 96$ and $\varepsilon = 5 \times 10^{-3}$. As in the case of $K_W^{(0)}$, the singular values decrease exponentially, indicating that dimensionality reduction can be used. It has also been made sure that the singular values of the kernel $K_W^{(1)}$ decrease exponentially for other combinations of N_τ and ε as well.

APPENDIX C: DETAILED FORMALISM FOR EXTRACTING SPECTRAL FUNCTIONS IN SPM

Here we explain a detailed formalism for extracting spectral functions in SpM.

The starting points of the formalism are Eqs. (1) and (2). Namely, the correlation function $G(\tau)$ is written as

$$G(\tau) = \int_0^\infty d\omega \frac{\cosh\left[\omega(\tau - \frac{1}{2T})\right]}{\sinh(\frac{\omega}{2T})}\rho(\omega). \tag{C1}$$

To treat it on a lattice whose spacing is a, it can be written in terms of dimensionless quantities as

$$\hat{G}(\hat{\tau}) = \int_0^\infty d\hat{\omega} \frac{\cosh\left[\hat{\omega}(\hat{\tau} - N_\tau/2)\right]}{\sinh\left(\hat{\omega}N_\tau/2\right)}\hat{\rho}(\hat{\omega}), \tag{C2}$$

where $\hat{\omega} \equiv \omega a$, $\hat{\tau} \equiv \tau/a$, $\hat{G} \equiv Ga^3$, $\hat{\rho} \equiv \rho a^2$ and N_τ is the extent of Euclidean times, respectively. As can be seen from the meaning of N_τ, $N_\tau a = 1/T$. Now we introduce $\hat{\omega}_{\max} \equiv \omega_{\max} a$ as a cutoff for $\hat{\omega}$ and normalize $\hat{\omega}$ and $\hat{\tau}$ by $\hat{\omega}_{\max}$ and N_τ respectively as follows:

$$\omega' \equiv \frac{\hat{\omega}}{\hat{\omega}_{\max}}, \qquad \tau' \equiv \frac{\hat{\tau}}{N_\tau}. \tag{C3}$$

Clearly, the ranges of these primed variables are $0 \le \omega' \le 1$ and $0 \le \tau' < 1$. Thus, with these primed variables, Eq. (C2) is written as

$$\hat{G}(\tau') = \int_0^1 d\omega' \hat{\omega}_{\max} \frac{\cosh\left[\omega'\Lambda(\tau' - 1/2)\right]}{\sinh\left(\omega'\Lambda/2\right)}\hat{\rho}(\omega'), \tag{C4}$$

where $\Lambda \equiv \hat{\omega}_{\max} N_\tau$. By discretizing the definite integral, turning it into a finite sum, and replacing $d\omega'$ with $\Delta\omega'$, the finite sum is given as

$$\hat{G}(\tau'_i) = \sum_{j=0}^{N_\omega - 1} \Delta\omega' \hat{\omega}_{\max} \frac{\cosh\left[\omega'_j\Lambda(\tau'_i - 1/2)\right]}{\sinh\left(\omega'_j/2\right)}\hat{\rho}(\omega'_j), \tag{C5}$$

where $\Delta\omega' \equiv 1/(N_\omega - 1)$ and N_ω is the number of points in ω-space. Note that $\omega'_0 = 0$ and $\tau'_0 = 0$.

Here we address two inconveniences. One is the lattice cutoff effects which appear correlation functions at short distances. To reduce it, we remove the first few points of the input data. The first point of Euclidean time after the removal is defined as τ'_{r} as the reference Euclidean time. The other is that the right-hand side of Eq. (C5) diverges at $\omega'_0 = 0$. To deal with it, we define

$$\tilde{\rho}(\omega'_j) \equiv \frac{\cosh\left[\omega'_j\Lambda(\tau'_{\mathrm{r}} - 1/2)\right]}{\sinh\left(\omega'_j\Lambda/2\right)}\hat{\rho}(\omega'_j). \tag{C6}$$

Rewriting Eq. (C5) using $\tilde{\rho}(\omega'_j)$, we obtain

$$\hat{G}(\tau'_i) = \sum_{j=0}^{N_\omega - 1} \Delta\omega' \hat{\omega}_{\max} \frac{\cosh\left[\omega'_j\Lambda(\tau'_i - 1/2)\right]}{\cosh\left[\omega'_j\Lambda(\tau'_{\mathrm{r}} - 1/2)\right]}\tilde{\rho}(\omega'_j). \tag{C7}$$

In Ref. [22], $\sqrt{\Delta\omega'}$ is included in the kernel to make the dependence of N_ω milder in the SpM analysis. We adopt it too and define the kernel as

$$K(\tau'_i, \omega'_j) \equiv \sqrt{\Delta\omega'}\hat{\omega}_{\max} \frac{\cosh\left[\omega'_j\Lambda(\tau'_i - 1/2)\right]}{\cosh\left[\omega'_j\Lambda(\tau'_{\mathrm{r}} - 1/2)\right]}. \tag{C8}$$

Rewriting the primed variables in Eq. (C8) into hatted variables yields Eq. (28).

APPENDIX D: ESTIMATION OF AN OPTIMAL VALUE OF λ

In this appendix we explain the estimation of an optimal value of λ, λ_{opt}. We employ the same method as in the previous study [22], which is summarized as follows:

(1) Fix a search range of λ as $[\lambda_{\min}, \lambda_{\max}]$ and divide the range into equal parts N_λ.
(2) Solve optimization problems using the squared error in IR basis, $\chi^2(\rho'_W(\hat{\omega}_j)|G'_W(\hat{\tau}_i))$, with various values of λ in the fixed range, $[\lambda_{\min}, \lambda_{\max}]$, by using ADMM algorithm [25] with the positivity constraint $\hat{\rho}(\omega'_i) \ge 0$.
(3) Connect the value of χ^2 at $\lambda_{\min}$ with that at $\lambda_{\max}$ by using a linear function on a logarithmic scale, $f(\lambda)$, since we obtain $\chi^2(\rho'_W(\hat{\omega}_j)|G'_W(\hat{\tau}_i))$ as a function of λ.

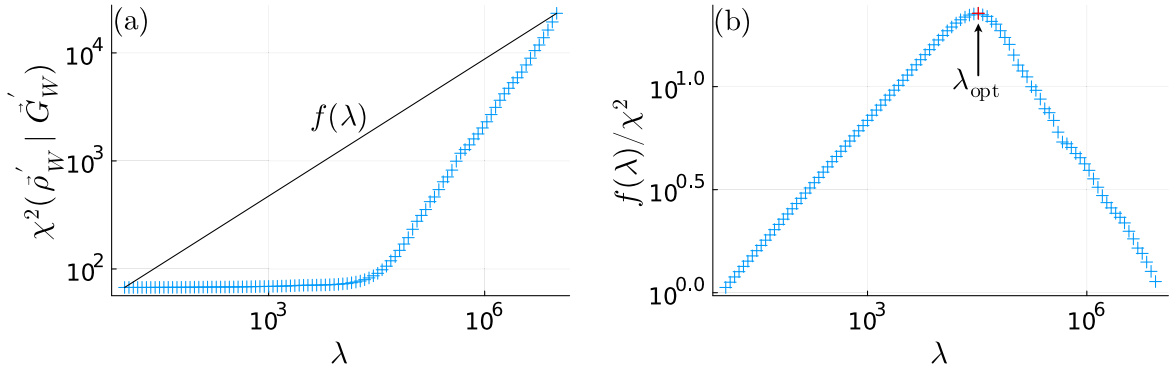

FIG. 12. An example of square error and $f(\lambda)/\chi^2$ in the mock-data test for $T > T_c$ with $N_\tau = 64$ and $\varepsilon = 10^{-5}$. (a) The square error in IR basis, $\chi^2(\rho'_W(\hat{\omega}_j)|G'_W(\hat{\tau}_i))$, as a function of λ. The function $f(\lambda)$ which is represented by the black solid line is defined as a linear function that connects the value of χ^2 at $\lambda_{\rm min}$ and that at $\lambda_{\rm max}$. This connection is expressed on a logarithmic scale. (b) $f(\lambda)/\chi^2$ as a function of λ, which means a reduction of χ^2 relative to $f(\lambda)$. The red plus sign denotes the peak of $f(\lambda)/\chi^2$ and represents the optimal value of λ, $\lambda_{\rm opt}$.

(4) Obtain $\lambda_{\rm opt}$ which produces the peak of $f(\lambda)/\chi^2$.

In our SpM analyses, N_λ is set at 100, and the range of $[\lambda_{\rm min}, \lambda_{\rm max}]$ is set to $[0.1, 10^7]$ for mock-data tests and $[1.0, 10^7]$ for analyses of lattice QCD data.

The $\lambda_{\rm opt}$ corresponds to the kink position in χ^2, and this position is the best place for the parameter λ of SpM [20]. Figure 12 shows an example of square error and $f(\lambda)/\chi^2$ in our mock-data test for $T > T_c$ with $N_\tau = 64$ and $\varepsilon = 10^{-5}$. Figure 12(a) shows the square error in IR basis, $\chi^2(\rho'_W(\hat{\omega}_j)|G'_W(\hat{\tau}_i))$, as a function of λ. The black solid line represents $f(\lambda)$. The purpose of the function $f(\lambda)$ is to accurately identify the kink position of χ^2 as a function of λ. Using this $f(\lambda)$, the peak position of $f(\lambda)/\chi^2$ corresponds to the kink position of χ^2, as shown in Fig. 12(b). In Fig. 12(b), the red plus sign denotes the peak of $f(\lambda)/\chi^2$ and represents the optimal value of λ, $\lambda_{\rm opt}$.

In our mock-data tests, $\lambda_{\rm opt}$ is estimated using the average value of 300 correlation functions created with Gaussian random numbers as error. These 300 correlation functions are created only for the purpose of calculating the covariance matrix. The statistical error of the spectral functions is not calculated in the mock-data tests for simplicity. Thus, there is only one $\lambda_{\rm opt}$ to be estimated for each combination of ε and N_τ. On the other hand, in the analyses of actual lattice QCD data, the statistical error of the spectral function is calculated using the jackknife method. In this method, jackknife samples are produced. While it is possible to determine $\lambda_{\rm opt}$ for each jackknife sample, the calculation of $\lambda_{\rm opt}$ is time-consuming. Furthermore, when an attempt was made to calculate $\lambda_{\rm opt}$ for each jackknife sample at a single temperature and for a single channel, it was found that the resulting $\lambda_{\rm opt}$ values were within the same order of magnitude, and the differences in the spectral function due to variations in $\lambda_{\rm opt}$ were found to be negligible. Consequently, as in the mock-data test, the mean value of the correlation function is utilized to calculate $\lambda_{\rm opt}$. This $\lambda_{\rm opt}$ is then used for each jackknife sample. Thus, there is only one $\lambda_{\rm opt}$ to be estimated for each combination of a temperature and a channel.

APPENDIX E: DETERMINATION OF μ AND μ'

The parameter μ is introduced to impose the constraint, $\vec{z} = V\vec{x}'$. As can be seen in the ADMM algorithm, the larger the magnitude of μ, the more vectors are updated to respect that constraint. Also, as expressed in Eqs. (A9), $\vec{z}$ is always positive definite. Therefore, satisfying $\vec{z} = V\vec{x}'$ is almost equivalent to satisfying the positivity of the spectral function $\vec{x}$ that we want to find.

It is not obvious what value of μ should be set to. Since we need to focus on the number of input data N_τ and the magnitude of noise ε in order to investigate the applicability of SpM in mock-data tests, we want to fix the value of μ. To this end, we have sought the optimal μ by calculating spectral functions for various values of μ. For simplicity,

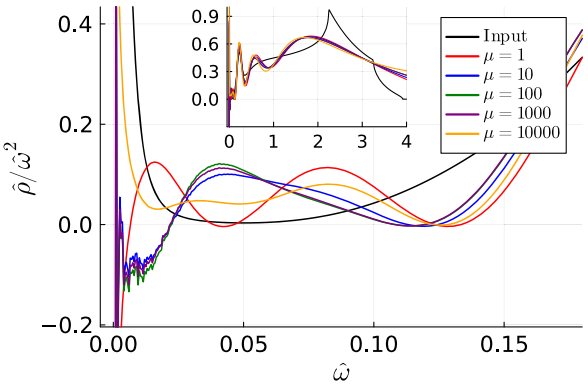

FIG. 13. Spectral functions in small value of $\hat{\omega}$ at various values of μ, which are obtained by using $K_W^{(0)}(\hat{\tau}_i, \hat{\omega}_j)$ in the mock-data test for $T > T_c$ with $N_\tau = 96$ and $\varepsilon = 10^{-2}$. The black line represents the input spectral function, and the red, blue, green, purple and yellow lines represent output results with $\mu = \mu' = 1$, 10, 100, 1000, 10000, respectively. These spectral functions in whole $\hat{\omega}$ region are drawn in small plot inside.

μ and μ' have been set to the same value in this study, and the following values for μ and μ' have been investigated: $\mu = \mu' = 10^i$ $(i = 0, 1, 2, 3, 4, 5)$.

As an example, we draw the spectral function at various values of μ in Fig. 13. Figure 13 shows spectral functions in small value of $\hat{\omega}$ obtained by using $K_W^{(0)}(\hat{\tau}_i, \hat{\omega}_j)$ in the mock-data test for $T > T_c$ with $N_\tau = 96$ and $\varepsilon = 10^{-2}$. The black line represents the input spectral function, and the red, blue, green, purple and yellow lines represent output results with $\mu = \mu' = 1, 10, 100, 1000, 10000$, respectively. These spectral functions in whole $\hat{\omega}$ region are drawn in small plot inside. When $\mu = 10^4$, it can be seen that the spectral function always has a positive value, while for other values, there are sections where it has a negative value. It is confirmed that the spectral function always has a positive value even when $\mu = 10^5$. However, when the value of μ is excessively large, a discernible peak in $f(\lambda)/\lambda$ is not evident, unlike Fig. 12(b). Consequently, it is not possible to estimate λ_{opt} appropriately. Thus it is determined that $\mu = 10^5$ is not suitable option.

The same investigation is conducted for all combinations of kernel $K_W^{(n)}$, N_τ, ε, and temperature T used in the mock-data test. As a result, it is determined that $\mu = \mu' = 10^4$ is optimal for both temperatures $T < T_c$ and $T > T_c$ when using $K_W^{(0)}$, and $\mu = \mu' = 10^3$ is optimal for $T < T_c$ when using $K_W^{(1)}$.

A thorough investigation is conducted using actual lattice QCD data, with $\mu = \mu' = 10^i$ $(i = 0, 1, 2, 3, 4)$ in order to ascertain the appropriate value of μ. Consequently, it is ascertained that the λ_{opt} is appropriately obtained for $\mu = \mu' = 10^i$ $(i = 2, 3, 4)$, and ensuring the preservation of the positivity of spectral function. Instead of setting the value of μ or μ' to a single value, the spectral function is obtained for $\mu = \mu' = 10^i$ $(i = 2, 3, 4)$ to estimate the systematic error.

[1] L. D. McLerran and T. Toimela, Photon and dilepton emission from the quark—gluon plasma: Some general considerations, Phys. Rev. D **31**, 545 (1985).

[2] E. Braaten, R. D. Pisarski, and T. C. Yuan, Production of soft dileptons in the quark-gluon plasma, Phys. Rev. Lett. **64**, 2242 (1990).

[3] G. D. Moore and J.-M. Robert, Dileptons, spectral weights, and conductivity in the quark-gluon plasma, arXiv:hep-ph/0607172.

[4] T. Matsui and H. Satz, J/ψ suppression by quark-gluon plasma formation, Phys. Lett. B **178**, 416 (1986).

[5] M. Laine, O. Philipsen, M. Tassler, and P. Romatschke, Real-time static potential in hot QCD, J. High Energy Phys. 03 (2007) 054.

[6] Y. Burnier, M. Laine, and M. Vepsäläinen, Heavy quarkonium in any channel in resummed hot QCD, J. High Energy Phys. 01 (2008) 043.

[7] Y. Burnier, O. Kaczmarek, and A. Rothkopf, Static quark-antiquark potential in the quark-gluon plasma from lattice QCD, Phys. Rev. Lett. **114**, 082001 (2015).

[8] D. Bala and S. Datta, Nonperturbative potential for the study of quarkonia in QGP, Phys. Rev. D **101**, 034507 (2020).

[9] S. Ali, D. Bala, O. Kaczmarek, and Pavan (HotQCD Collaboration), Thermal static potential and pseudoscalar quarkonium spectral functions from $(2+1)$-flavor lattice QCD, Phys. Rev. D **112**, 054510 (2025).

[10] A. Adare *et al.* (PHENIX Collaboration), J/ψ production vs centrality, transverse momentum, and rapidity in Au + Au collisions at $\sqrt{s_{NN}} = 200$ GeV, Phys. Rev. Lett. **98**, 232301 (2007).

[11] A. Adare *et al.* (PHENIX Collaboration), Measurement of $\Upsilon(1S + 2S + 3S)$ production in $p + p$ and Au + Au collisions at $\sqrt{s_{NN}} = 200$ GeV, Phys. Rev. C **91**, 024913 (2015).

[12] J. Adam *et al.* (ALICE Collaboration), J/ψ suppression at forward rapidity in Pb-Pb collisions at $\sqrt{s_{\text{NN}}} = 5.02$ TeV, Phys. Lett. B **766**, 212 (2017).

[13] S. Acharya *et al.* (ALICE Collaboration), Υ suppression at forward rapidity in Pb-Pb collisions at $\sqrt{s_{\text{NN}}} = 5.02$ TeV, Phys. Lett. B **790**, 89 (2019).

[14] A. M. Sirunyan *et al.* (CMS Collaboration), Measurement of nuclear modification factors of $\Upsilon(1S)$, $\Upsilon(2S)$, and $\Upsilon(3S)$ mesons in PbPb collisions at $\sqrt{s_{\text{NN}}} = 5.02$ TeV, Phys. Lett. B **790**, 270 (2019).

[15] P. Petreczky and D. Teaney, Heavy quark diffusion from the lattice, Phys. Rev. D **73**, 014508 (2006).

[16] M. Asakawa, Y. Nakahara, and T. Hatsuda, Maximum entropy analysis of the spectral functions in lattice QCD, Prog. Part. Nucl. Phys. **46**, 459 (2001).

[17] B. B. Brandt, A. Francis, H. B. Meyer, and D. Robaina, Pion quasiparticle in the low-temperature phase of QCD, Phys. Rev. D **92**, 094510 (2015).

[18] S. Hashimoto, Inclusive processes from lattice QCD: problems and opportunities, in *Proceedings of the 16th Conference on Quark Confinement and the Hadron Spectrum* (2025), arXiv:2503.23023.

[19] H.-T. Ding, O. Kaczmarek, S. Mukherjee, H. Ohno, and H.-T. Shu, Stochastic reconstructions of spectral functions: Application to lattice QCD, Phys. Rev. D **97**, 094503 (2018).

[20] J. Otsuki, M. Ohzeki, H. Shinaoka, and K. Yoshimi, Sparse modeling approach to analytical continuation of imaginary-time quantum Monte Carlo data, Phys. Rev. E **95**, 061302 (2017).

[21] H. Shinaoka, J. Otsuki, M. Ohzeki, and K. Yoshimi, Compressing Green's function using intermediate representation between imaginary-time and real-frequency domains, Phys. Rev. B **96**, 035147 (2017).
[22] E. Itou and Y. Nagai, Sparse modeling approach to obtaining the shear viscosity from smeared correlation functions, J. High Energy Phys. 07 (2020) 007.
[23] J. Otsuki, M. Ohzeki, H. Shinaoka, and K. Yoshimi, Sparse modeling in quantum many-body problems, J. Phys. Soc. Jpn. **89**, 012001 (2020).
[24] S. Boyd and L. Vandenberghe, *Convex Optimization* (Cambridge University Press, Cambridge, England, 2004).
[25] S. Boyd, N. Parikh, E. Chu, B. Peleato, and J. Eckstein, Distributed optimization and statistical learning via the alternating direction method of multipliers, Found. Trends ® Mach. Learn. **3**, 1 (2011).
[26] F. Karsch, E. Laermann, S. Stickan, and P. Petreczky, Infinite temperature limit of meson spectral functions calculated on the lattice, Phys. Rev. D **68**, 014504 (2003).
[27] G. Aarts and J. M. Martínez Resco, Continuum and lattice meson spectral functions at nonzero momentum and high temperature, Nucl. Phys. **B726**, 93 (2005).
[28] J. Takahashi, H. Ohno, and A. Tomiya, Sparse modeling approach to extract spectral functions with covariance of Euclidean-time correlators of lattice QCD, Proc. Sci. LATTICE2023 (**2023**) 028.
[29] H.-T. Ding, A. Francis, O. Kaczmarek, F. Karsch, H. Satz, and W. Soeldner, Charmonium properties in hot quenched lattice QCD, Phys. Rev. D **86**, 014509 (2012).